On the use of metasurface for Vortex-Induced vibration suppression or energy harvesting

Junlei Wang [a,b], Shaokang Sun [a], Lihua Tang [b,*], Guobiao Hu [b,c,*], Junrui Liang [c]

[a] School of Mechanical and Power Engineering, Zhengzhou University, Zhengzhou 450000, China
[b] Department of Mechanical Engineering, The University of Auckland, Auckland 1010, New Zealand
[c] School of Information Science and Technology, ShanghaiTech University, Shanghai 201210, China

ARTICLE INFO

ABSTRACT

This paper explores the use of metasurface in designing an aerodynamic system for potential vortex-induced vibration (VIV) suppression or energy harvesting. Four kinds of metasurface patterns are designed to decorate an ordinary cylinder bluff body for modifying its aerodynamic characteristics. A theoretical model is developed for the VIV system by describing the wake as a van der Pol oscillator. The aerodynamic parameters, i.e., the lift and drag coefficients, used in the theoretical model, are determined from three-dimensional CFD simulations. A wind tunnel experiment is conducted to validate the theoretical model and investigate the aerodynamic behaviors of the VIV systems with different bluff bodies. It is found that the metasurface pattern has a significant influence on the aerodynamic characteristics of the bluff body. Using different metasurface patterns to decorate the bluff body, the vortex-induced vibration of the system could be either enhanced or suppressed, compared with the baseline reference using an ordinary bluff body with a smooth surface. Furthermore, the vortex shedding processes are simulated to give further insights into the wake oscillating motions. The roles of the metasurface in suppressing or enhancing the vortex-induced vibration are reasonably explained: the existence of metasurfaces could alter the flow field around the bluff bodies and consequently the aerodynamic force. In addition, based on the validated theoretical model, it is learned from a parametric study that the power output reaches saturation when the electromechanical coupling strength is increased to a certain level. Therefore, piezoelectric transducers with moderate coupling coefficients are recommended for practical applications from the cost-effective perspective.

1. Introduction

Wireless sensor networks (WSN) and micro-electro-mechanical-systems (MEMS) have been rapidly developed in the context of the fourth industrial revolution that aims to connect all the physical assets through Internet of Things (IoT). After the deployment, the maintenance of the large-scale WSN puts forward an urgent demand for a sustainable power supply to realize perpetual operation. In the past two decades, energy harvesting technology has been proposed by researchers to harness energy from ambient sources such as solar, thermal, vibration, wind, etc. Due to technological innovation, the power consumption of up-to-date devices has been significantly reduced. Therefore, energy harvesting technology becomes a viable solution to meet the afore-mentioned power supply requirements [1–8].

Wind, as a ubiquitous source in nature, has been widely recognized as important renewable energy [9]. To make use of wind energy, besides traditional methods using windmill-like turbo-machineries for large-scale power generation, various flow-induced vibration (FIV) phenomena have been exploited in recent years for small-scale energy harvesting [10,11]. According to the aerodynamic mechanisms behind different phenomena, FIVs can be classified into vortex-induced vibration (VIV) [12–14], galloping [15–17], flutter [18,19], wake galloping [20,21]. To subsequently convert the induced vibrations into electricity, common energy transduction methods, including electrostatic [22,23], electro-magnetic [24,25], piezoelectric [26–31], triboelectric transducers [32–34] can be utilized. Because of the high power density and the ease of implementation, piezoelectric transduction is the most widely used for energy harvesting. A typical piezoelectric wind energy harvester can be obtained by attaching a bluff body to a piezoelectric cantilever beam.

Vortex-induced vibration is a typical FIV phenomenon resulting from the self-excited oscillation caused by fluid–structure interaction (FSI)

Nomenclature

U	Wind speed
D	Diameter of the cylinder bluff body
L_0, L_p, L_b	Length of the bluff body, piezoelectric sheet, cantilever beam
W_p, W_b	Width of the piezoelectric sheet, cantilever beam
T_p, T_b	Thickness of the piezoelectric sheet, cantilever beam
$\eta(t)$	Modal coordinate
$\dot{\eta}(t)$	Velocity of the modal coordinate
$\ddot{\eta}(t)$	Acceleration of the modal coordinate
ξ	Damping ratio
ω_n	Natural frequency
$V(t)$	Voltage across the piezoelectric transducer
χ	Modal electromechanical coupling coefficient
R_L	Resistive load
C_p	Clamped capacitance of the piezoelectric transducer
$F_{VIV}(t)$	Vortex-induced aerodynamic force
C_L	Fluctuating lift coefficient
C_{L0}	Amplitude of the fluctuating lift force coefficient
C_{Lrms}	Root mean square (RMS) value of lift coefficient
C_D	Mean drag coefficient
$\varphi(L_b)$	Fundamental mode shape of the cantilever beam
ρ	Air density
$q(t)$	Variable to describe the motion of the near wake of the flow past the bluff body
λ, A	Modal constants
ω_s	Vortex shedding frequency
M_{eff}	Equivalent mass
C_{eff}	Equivalent damping
K_{eff}	Equivalent stiffness
$u(t)$	Displacement of the tip of the cantilever beam
$f_i(\boldsymbol{x}, t)$	Particle distribution function with real variables
c_i	Velocity component
Δt	Time step
Ω_i	Collision operator
$1/\tau$	Collision frequency
$f_i^{(eq)}$	Local equilibrium function of the macroscopic properties of the flow
$\vec{u}$	Macroscopic velocity of fluid
w_i	Weight constants built to preserve the isotropy
δ	Kronecker delta
$\vec{e_i}$	Discrete set of velocities
c_s	Lattice sound speed
R	Gas constant
T	Macroscopic temperature
L_1	Characteristic length of the convex parts
θ	Electromechanical coupling coefficient
S_t	Strouhal number
$\overline{P}_{avg}$	Averaged power
k_e^2	Electromechanical coupling strength

[35–37]. To improve and optimize the performance of a VIV-based energy harvester, numerous theoretical and experimental studies have been conducted by researchers. Dai et al. [38] developed a distributed parameter model of a VIV-based piezoelectric energy harvester (PEH) and conducted a parametric study to reduce the cut-in wind speed. Azadeh-Ranjba et al. [39] revealed that reducing the aspect ratio of a finite-length cylinder could broaden the "lock-in" region of VIV and increase the vibration amplitude of the system, thus leading to broadband energy harvesting with enhanced power output.

Besides, researchers have devoted efforts to modifying the topological structures of bluff bodies to improve the energy harvesting performance. Based on the concept of passive turbulence control (PTC) proposed by Bernitsas et al. [40], Wang et al. [41] investigated the performance of a piezoelectric wind energy harvester under passive turbulence control. It was proved that the employment of the PTC strategy could significantly widen the operating wind speed range and increase the power output of the energy harvester. Wang et al. [42] proposed a novel bluff body with "Y-shaped" attachments for a VIV-based PEH. It was found that by adding Y-shaped attachments to an ordinary cylinder, there appeared a VIV-to-galloping transition phenomenon, which significantly improved the energy harvesting performance. Hu et al. [43] attached two rods on the cylinder bluff body of a wind energy harvester to modify the aerodynamic characteristics of the system for realizing energy harvesting over a wide range of wind speeds. He et al. [44] developed a wind energy harvester with a VIV and galloping merged region. The interaction between VIV and galloping was experimentally found to be a practical approach to improve the efficiency of the energy harvester at low wind speeds. Relevant research based on similar ideas was conducted by Sun et al. [45] and Wang et al. [46] as well. On the other hand, FIVs may often cause harmful fatigue damage to structures and need to be avoided in many engineering situations. For example, in an experimental study, Song et al. [47] arranged three auxiliary control rods evenly around the riser model to reduce the VIV response of the riser, so as to decrease the damage caused by VIV and increase the service life of the riser structure. To explore the mechanism of vibration reduction, Zhu et al. [48] added two small

rotating control rods near the wake of the vibrating cylinder. Based on numerical simulations, they found that the amplitude of the vibrating cylinder could be effectively suppressed. Vortex-induced vibration is like a two-edged sword. The "lock-in" phenomenon could be beneficial for energy harvesting, but also harmful to the safety of engineering structures in the meantime. Therefore, the "lock-in" phenomenon should be carefully treated. Depending on the purpose of suppressing VIV to ensure structural safety or enhancing VIV to improve energy harvesting performance, a system should be appropriately tuned to tailor the VIV "lock-in" region.

According to the literature review, the topological structure of a bluff body plays an important key role in affecting the aerodynamics of a VIV system. In recent years, due to the unique properties of periodic metasurfaces, they have been widely used in various disciplines, e.g., the optics [49,50], acoustics [51,52], and seismology [53,54]. Mou et al. [55] proposed an illuminator based on optical metasurface etched with rectangular nanoholes on silver films. By changing the arrangement of rectangular holes, the shape and layout of the light spots could be adjusted. The metasurface array illuminator had the advantages of ultrathin thickness and compact structure, making it conducive to the application in optical interconnection and integration. Long et al. [56] showed that ultrathin sponge coating could achieve efficient absorptions if backed by a metasurface with a moderate surface impedance. By coupling the ultra-thin sponge coating with the designed metasurface, it was theoretically and experimentally proved that the deep sub-wavelength broadband absorber has a high absorption rate (>80%) over the frequency range from 185 Hz to 385 Hz. Their research provided a practical way to develop broadband low-frequency sound absorbers. He et al. [57] investigated a new method of seismic Rayleigh wave process using phase-gradient metasurfaces. The numerical results demonstrated that the Rayleigh wave could be focused, split, or converted into evanescent waves by utilizing the special phase-gradient metasurface structures. Therefore, the metasurface had great potential in shielding seismic surface waves.

In various disciplines, it has been proved that metasurface (i.e., periodic microstructures) could possibly bring a significant influence and
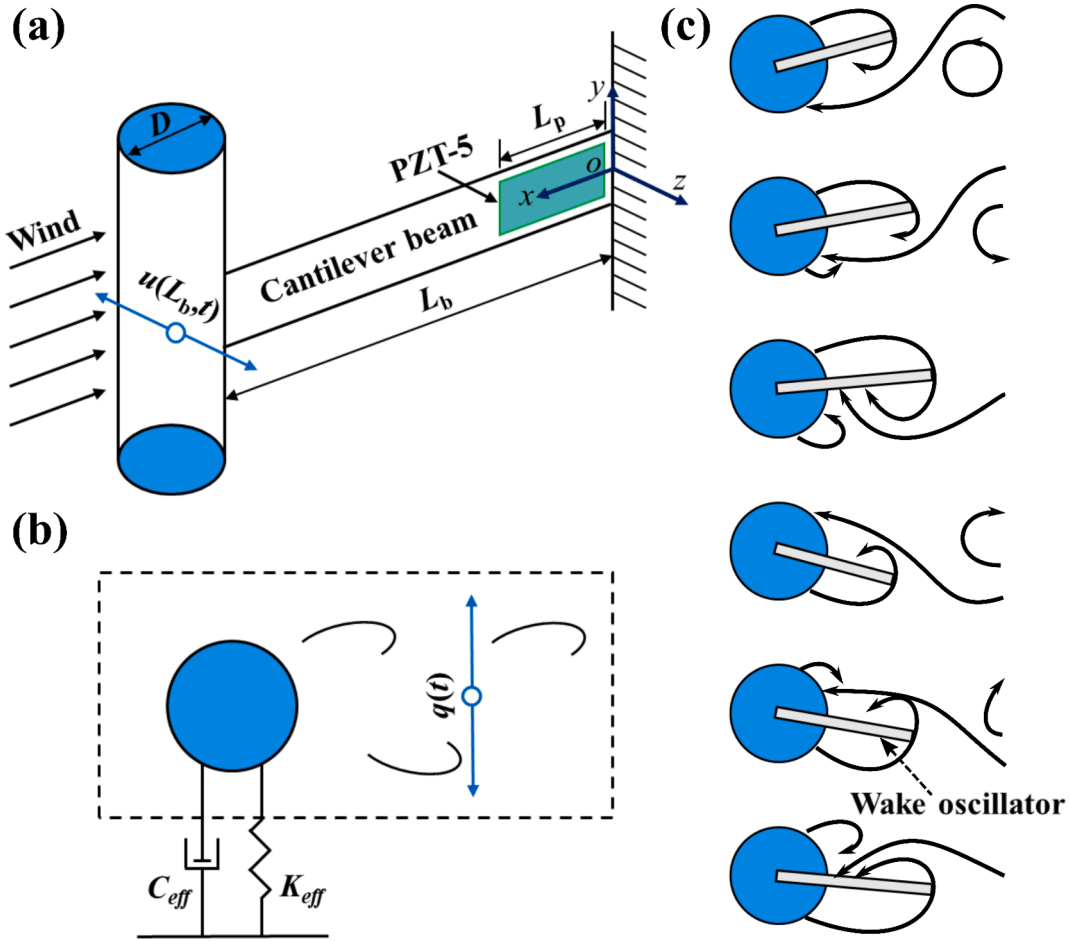
Fig. 1. (a) Schematic of VIVPEH; (b) equivalent lumped parameter model of VIVPEH; (c) illustration of the mechanism of the wake oscillator model.

extraordinarily improve the system performance. At the same time, in retrospect to the work by Wang *et al.* [42] that the introduction of attachments on bluff bodies could enhance the power output of the wind energy harvester, it is thus inspired to explore the possibility of introducing the concept of metasurface, which is actually the idea of periodic attachments, into the design of an aerodynamic system. According to the literature review, in the aerodynamic field, using metasurface to design a system for VIV-based energy harvesting or VIV control has not been found yet. Inspired by the aforementioned studies for VIV enhancement or suppression using modified bluff bodies, this paper explores the idea of introducing several periodic metasurface patterns to decorate ordinary bluff bodies. Four kinds of metasurface patterns, namely, convex hemisphere, convex tri-prism, convex cylinder, and convex prism, are investigated in this paper. A general theoretical model of a VIV-based piezoelectric energy harvester (PEH) is developed in Section 2. The synergy of three-dimensional CFD simulation and analytical model is specifically for the modeling and computation of the proposed VIV system with metasurfaces. The physical prototypes and experimental setup are introduced in Section 3. In Section 4, the theoretical and experimental results are compared for validating the theoretical model. Moreover, the experimental results are discussed in detail to provide guidelines on the use of different metasurfaces towards vortex-induced vibration suppression or energy harvesting. In Section 5, CFD simulation results are used to explain the roles of different metasurfaces in affecting the vortex shedding processes of the bluff bodies. In addition, based on the theoretical model, a parametric study is performed to investigate the effects of the resistive load and the electromechanical coupling strength on the energy harvesting performance of the system. The conclusions are summarized in Section 6.

2. Modeling

2.1. Lumped parameter model

Fig. 1 shows the schematic of the VIV-based piezoelectric energy harvester (VIVPEH). The cantilever beam, together with the cylinder bluff body, oscillates transversely in the z-direction driven by the aerodynamic force under a uniform wind flow with a constant speed of U. The cylinder bluff body has a length of $L_0 = 120$ mm and a diameter of $D = 35$ mm. A piezoelectric sheet (PZT-5) with dimensions of $L_p \times W_p \times T_p = 30$ mm $\times$ 20 mm $\times$ 0.5 mm is attached to the cantilever beam with dimensions of $L_b \times W_b \times T_b = 185$ mm $\times$ 20 mm $\times$ 0.5 mm.

Based on Euler's beam theory [58] and keeping only the fundamental mode, the dynamic behavior of the lumped model of the piezoelectric cantilever subjected to an aerodynamic force is governed by the following equation:

$$\ddot{\eta}(t) + 2\xi\omega_n\dot{\eta}(t) + \omega_n^2\eta(t) + \chi V(t) = F_{VIV}(t) \tag{1}$$

where $\eta(t)$ is the modal coordinate; ξ is the damping ratio of the fundamental mode; ω_n is the fundamental natural frequency; $V(t)$ is the voltage across the piezoelectric transducer and χ is the modal electromechanical coupling coefficient. Assuming that the piezoelectric transducer is shunted to a simple resistive load R_L, the circuit equation can be written as:

$$\frac{V(t)}{R_L} + C_p\dot{V}(t) - \chi\dot{\eta}(t) = 0 \tag{2}$$

where C_p is the clamped capacitance of the piezoelectric transducer. The vortex-induced aerodynamic force in Eq. (1) can be expressed as:

$$F_{VIV}(t) = \frac{1}{2}\rho C_L D U^2 L_0 - \frac{1}{2}\rho C_D D U L_0 \varphi^2(L_b)\dot{\eta}(t) \tag{3}$$

where $C_L = (C_{L0}/2)q(t)$ represents the fluctuating lift coefficient. C_{L0} is the amplitude of the fluctuating lift force coefficient applied on the stationary bluff body and C_D is the mean drag coefficient, which can be obtained from CFD simulation. $\varphi(x)$ is the fundamental mode shape of the cantilever beam. ρ is the air density. $q(t)$ is the variable to describe the motion of the near wake of the flow past the bluff body. To reflect the effect of the flow wake on the dynamics of the bluff body, the variable $q(t)$ is introduced in the lift force term that acts on the bluff body. The dynamic motion of the flow wake is assumed to follow the behavior of a van del Pol oscillator. The governing equation of $q(t)$ can thus be expressed as

$$\ddot{q}(t) + \lambda\omega_s\left[q^2(t) - 1\right]\dot{q}(t) + \omega_s^2 q(t) = \frac{A}{D}\varphi(L_b)\ddot{\eta}(t) \tag{4}$$

where λ and A can be determined experimentally, which are equal to 0.3 and 12, respectively [59]. ω_s is the vortex shedding frequency:

$$\omega_s = \frac{2\pi S_t U}{D} \tag{5}$$

After re-arranging Eq. (1) to satisfy the assumption that the lumped parameters are concentrated at the tip of the cantilever beam, one obtains:

$$M_{eff} = 1/\varphi^2(L_b), C_{eff} = 2\xi\omega_n/\varphi^2(L_b), K_{eff} = \omega_n^2/\varphi^2(L_b), \theta = \chi/\varphi(L_b), u(t)$$
$$= \varphi(L_b)\eta(t)$$

where M_{eff}, C_{eff}, K_{eff} are the equivalent mass, damping coefficient, and stiffness, respectively. $u(t)$ is the displacement of the tip of the cantilever beam. Eqs. (1), (2), (4) can then be rewritten as:

$$M_{eff}\ddot{u}(t) + \left[C_{eff} + \frac{1}{2}\rho C_D D U L_0\right]\dot{u}(t) + K_{eff}u(t) + \theta V(t) = \frac{1}{4}\rho C_{L0} D U^2 L_0 q(t) \tag{6}$$

$$\frac{V(t)}{R_L} + C_p\dot{V}(t) - \theta\dot{u}(t) = 0 \tag{7}$$

$$\ddot{q}(t) + \lambda\omega_s\left[q^2(t) - 1\right]\dot{q}(t) + \omega_s^2 q(t) = \frac{A}{D}\ddot{u}(t) \tag{8}$$

The rigorous procedure to determine the equivalent lumped parameters is by computing the fundamental mode shape of the cantilever beam. Alternatively, a convenient means to determine the lumped parameters can be through an experiment [60]. Regarding the aerodynamic parameters, the lift and drag coefficients of a specific bluff body could be identified from a series of wind tunnel experiments or CFD simulations. In this study, to assist the fast development of the theoretical model, the aerodynamic coefficients are computed from CFD simulations. Once C_{L0} and C_D are obtained from CFD simulations, the response of the bluff body and the corresponding electrical output can be simulated with Eqs. (6)–(8) written in the state space form. The theoretical results will be finally validated by the experiment.

2.2. Three-dimensional CFD model

In this section, the CFD platform XFlow based on the Lattice-Boltzmann method (LBM) is used to carry out three-dimensional (3D) simulations for the stationary bluff body. Different from the traditional CFD method, the LBM does not solve the Navier-Stokes equation of the fluid, but calculates the streaming and collision between microscopic particles. Hence, the LBM method adopts a simpler description of fluid interaction, making it easier to consider complex boundaries and implement parallel calculation. The Boltzmann transport equation is normally written as follows:

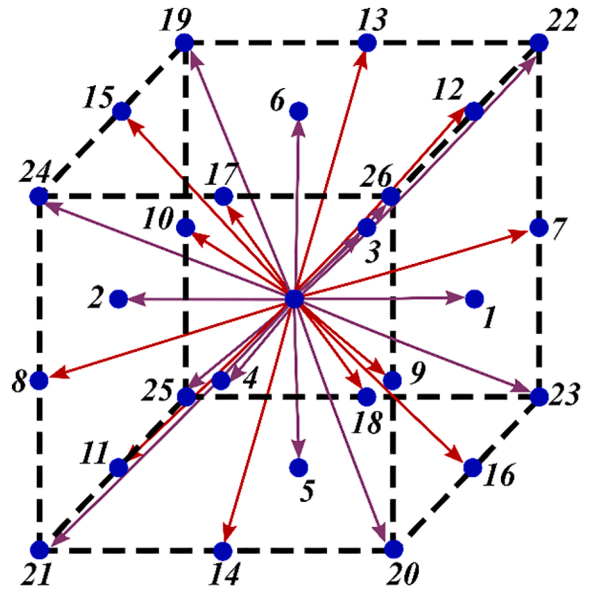$$f_i(x + c_i\Delta t, t + \Delta t) = f_i(x, t) + \Omega_i[f(x, t)] \tag{9}$$

Fig. 2. Velocity components of the D3Q27 model.

where the subscript i equals to 0, 1, ..., 26 in D_3Q_{27} model and $f_i(x, t)$ is the particle distribution function with real variables, reserving by constructing the conservation of mass, linear momentum and energy, c_i is the velocity component in one of the predetermined directions of the i-th particle; Δt is the time step; Ω_i stands for the collision operator, which indicates the change rate of the particle distribution function caused by the collision.

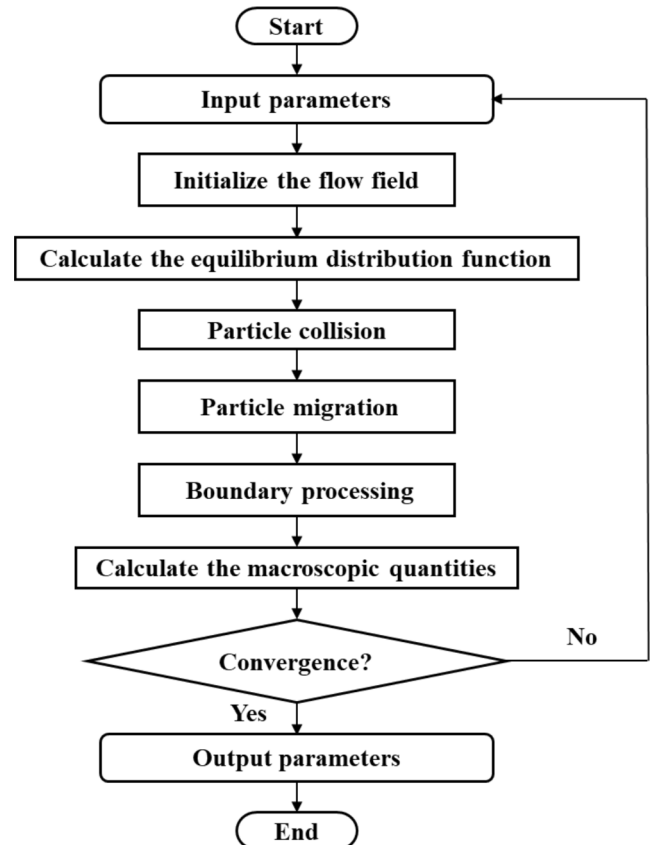By introducing the BGK model proposed by Bhatnagar, Gross and

Fig. 3. The solution process of the Lattice-Boltzmann method (LBM).

Table 1
Parameters of the incoming flow ($T = 288.15$ K).

Parameters	Values/Units
Thermal conductivity	0.0243 W/(m·K)
Density	1.2041 kg/m³
Viscosity	1.7894e−5 Pa·s
Molecular weight	28.99 kg /kmol
Specific heat capacity	1006.43 J/(kg·K)

Krook [61] in 1954, the collision operator can be expressed in the following formula:

$$\Omega_i = -\frac{1}{\tau}\left[f_i(x,t) - f_i^{(eq)}(x,t)\right] \tag{10}$$

where $1/\tau$ is the collision frequency. Fig. 2 shows the three-dimensional D3Q27 model consisting of 27 discrete velocity directions. $f_i^{(eq)}$ is the local equilibrium function of the macroscopic properties of the flow and can be expressed as:

$$f_i^{(eq)} = \rho w_i\left(1 + \frac{u_\alpha e_{i\alpha}}{c_s^2} + \frac{u_\alpha u_\beta e_{i\alpha} e_{i\beta}}{2c_s^4} - \frac{u_\alpha u_\beta \delta_{\alpha\beta}}{2c_s^2}\right) \tag{11}$$

where ρ and $\vec{u}$ are the macroscopic density and the velocity of fluid, respectively; w_i is the weight constants built to preserve the isotropy [61]; δ is the Kronecker delta; $\vec{e_i}$ is the discrete set of velocities. The subscript α and β stand for the different spatial components of vectors in the equation. c_s is the lattice sound speed.

$$c_s = \sqrt{RT} \tag{12}$$

where R and T are the gas constant and the macroscopic temperature, respectively.

To analyze the external force $F_{VIV}(t)$, the pressure distributed around the bluff body needs to be computed. By integrating the pressure, the lift and drag coefficients can be obtained. To restore the macroscopic equation, the equilibrium distribution function must satisfy the conservation of the mass and the momentum:

$$\rho = \sum_i f_i = \sum_i f_i^{(eq)} \tag{13}$$

$$\rho\vec{u} = \sum_i c_i f_i = \sum_i c_i f_i^{(eq)} \tag{14}$$

The solution process of LBM is illustrated in Fig. 3. The pressure can be obtained by

$$P = \rho c_s^2 \tag{15}$$

Based on the iterative computations shown in Fig. 3, the lift and drag coefficients can be calculated. To ensure the convergence of the following numerical calculation, a fixed three-dimensional cylinder being placed in an incoming flow with $U = 2.509$ m/s is first simulated. The parameters of the flow are listed in Table 1. The flow mode is set as the external single-phase and enforced incompressible model in a virtual

Table 2
Geometric parameters of the flow field calculation domain ($D = 35$ mm).

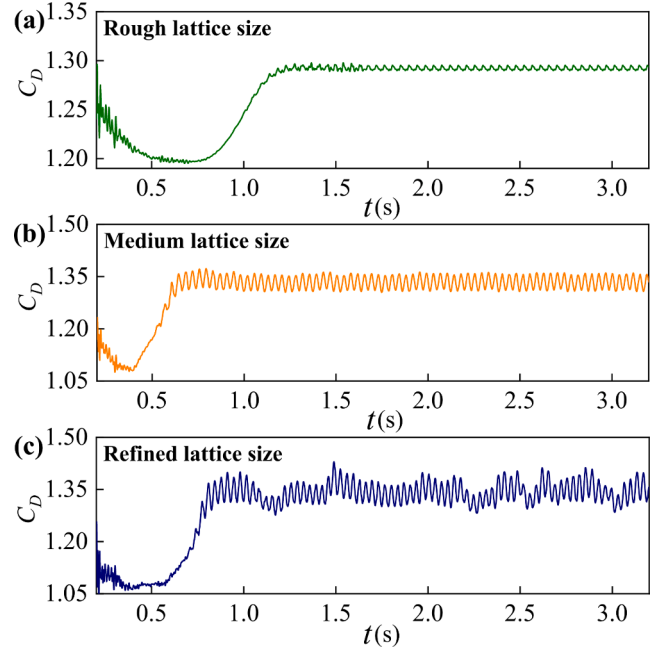| X_u/D	X_d/D	Y/D	Z/D
10	25	3.43	20

Fig. 5. The time history responses of the drag coefficient simulated by CFD: (a) rough lattice size (temporal-averaged C_D = 1.292); (b) medium lattice size (temporal-averaged C_D = 1.331); (c) refined lattice size (temporal-averaged C_D = 1.341).
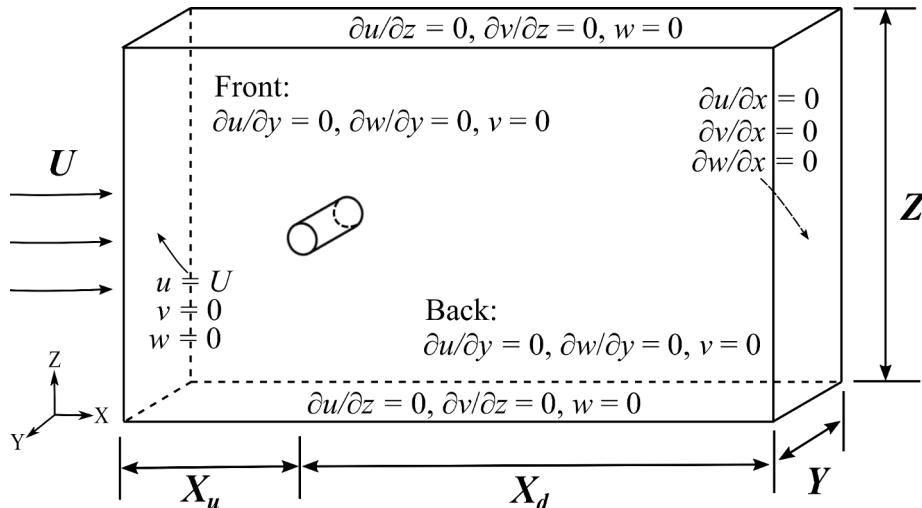

Fig. 4. Configuration of the computation domain and boundary conditions.

Table 3

The resolution convergence study results.

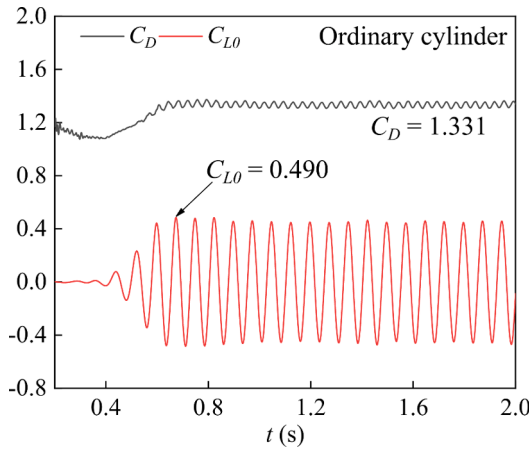| Lattice size	C_D	C_{Lrms}
Rough	1.292	0.279
Medium	1.331	0.323
Refined	1.341	0.334

Fig. 6. Identification of C_{L0} and C_D from their time history responses.

wind tunnel. Fig. 4 presents the configuration of the computation domain and boundary conditions. The geometric parameters of the flow field calculation domain are listed in Table 2. The left and right ends of the computation domain are, respectively, set as velocity inlet and flow outlet. The symmetric boundary condition is applied to the lateral surface of the computation domain. The bluff body's surface and the rest of the boundaries are set as stationary walls. The Smagorinsky turbulence model of large eddy simulation function providing by XFlow is adopted to carry out the turbulence simulation. The Smagorinsky turbulence model has reasonable accuracy when calculating the aerodynamic characteristics [62].

Three different resolutions ($D/25$, $D/35$, $D/50$), which are referred as rough, medium, and refined sizes, respectively, near the bluff body have been examined. Their number of elements of the numerical mesh are 695,440, 1,767,810 and 5,020,162, respectively. In the present work, the time step size is self-adaptive. The target resolution scale is four times more precise than the global resolved scale. Fig. 5 shows the drag coefficient time-history curves for the cases using rough, medium, and refined lattice sizes, respectively. Besides, Table 3 lists the mean value of the drag coefficient C_D and the root mean square (RMS) value of lift coefficient C_{Lrms}. It can be noted that the computational results of C_D and C_{Lrms} gradually converge and the divergences gradually decrease. To make a compromise between the computing resources and accuracy, the medium lattice size has been chosen in the following CFD simulation. Similarly, the amplitude of the fluctuating lift coefficient C_{L0} in Eq. (3) can be identified through the above simulation process as well. The corresponding time-history curve of the lift coefficient for the example case is shown in Fig. 6.

The convergence study has successfully validated that the lattice size is sufficiently refined to ensure the simulation accuracy. Thus numerical calculations for different bluff bodies can be conducted to identify their aerodynamic coefficients. In this work, four metasurface patterns, namely, convex hemisphere (Convex H), convex tri-prism (Convex T), convex cylinder (Convex C), and convex prism (Convex P), are used to decorate the cylinder bluff bodies, as shown in Fig. 7. The convex parts are arranged in the same way, with 8 protrusions in each column along the circumference at a uniform interval. The characteristic length L_1 of the convex parts is 6 mm. The height of the convex parts is 3 mm. The longitudinal center distance between the two convex parts is 14 mm.
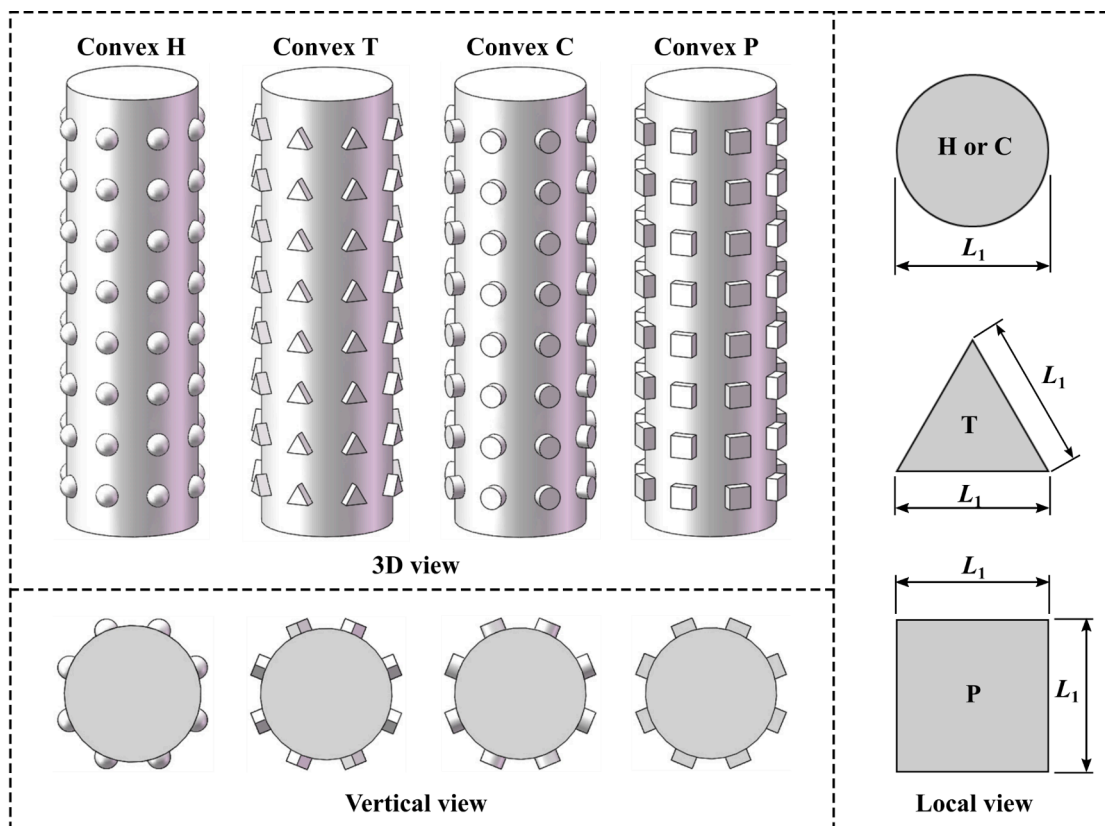

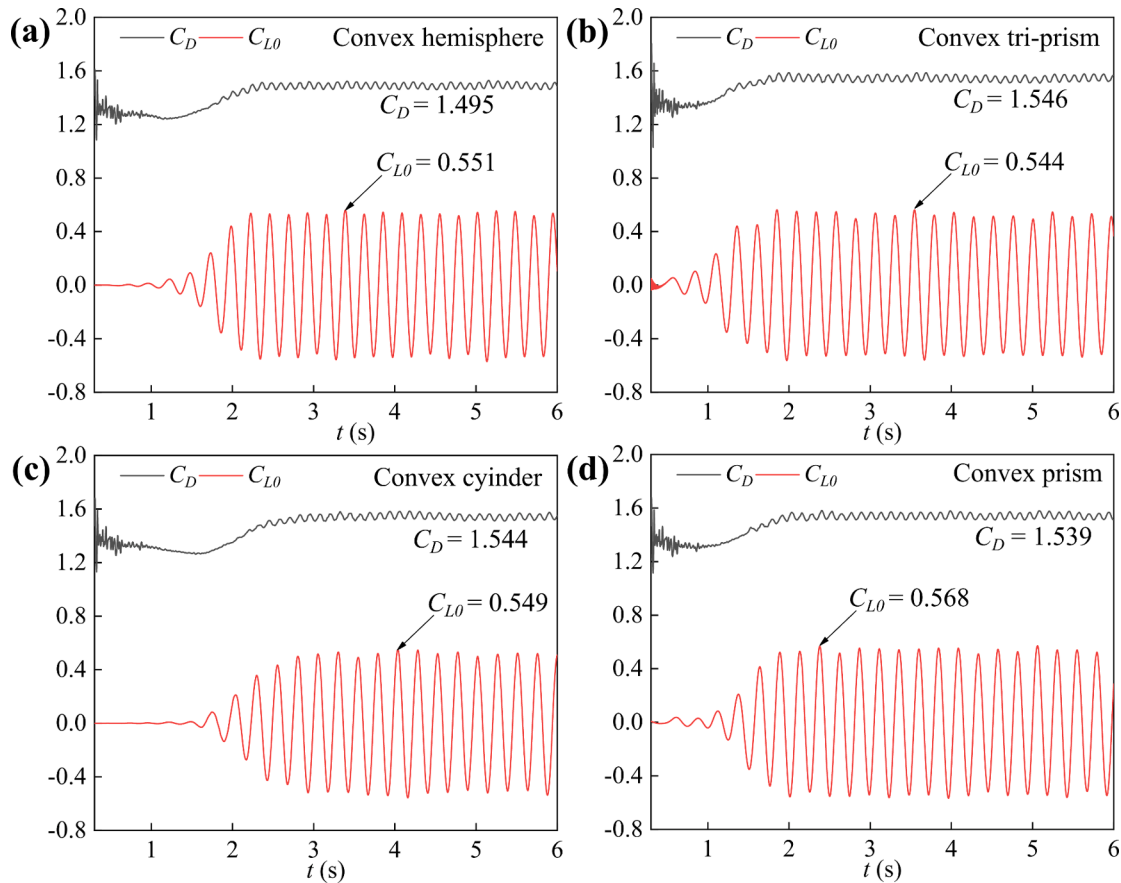**Fig. 7.** The bluff bodies decorated by various metasurface patterns.

Fig. 8. Time history responses of C_{L0} and C_D for bluff bodies with various metasurface patterns: (a) convex hemisphere; (b) convex tri-prism; (c) convex cylinder; (d) convex prism.
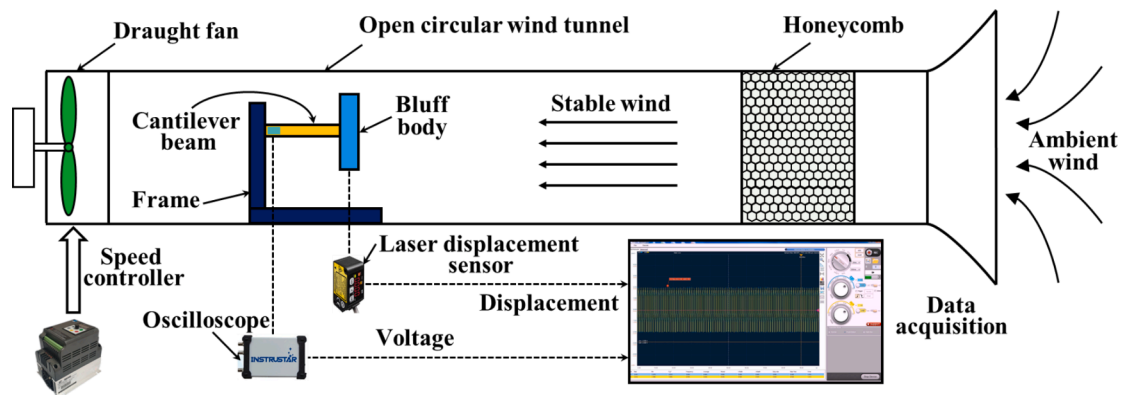

Fig. 9. The schematic of the wind tunnel experimental platform.

Fig. 8 demonstrates the identified C_{L0} and C_D for bluff bodies with various metasurfaces.

3. Prototypes and experimental setup

Fig. 9 presents the architecture of the wind tunnel experimental platform. Fig. 10 demonstrates the proposed prototypes with bluff bodies decorated by various metasurfaces. The wind tunnel system is constituted by a circular tunnel, a draught fan, a two-sectioned honeycomb structure and a data acquisition facility. The VIVPEH consists of a piezoelectric cantilever beam and a bluff body. The cantilever beam and bluff body are made of aluminum and foam materials, respectively. The whole structure of the VIVPEH is installed in the open circular wind

tunnel with a diameter of 400 mm. The wind tunnel is made of organic glass. By controlling the frequency converter to change the rotational speed of the draught fan, different wind speeds can be achieved in the wind tunnel. The conversion relation between wind speed and frequency can be expressed as $U = 0.137f + 0.18$. Due to the controller performance, the command resolution of the rotation speed of the draught fan is limited to the accuracy level of revolutions per minute. The honeycomb structure is used to stabilize the ambient wind to meet the experimental requirements. The voltage generated by the piezoelectric transducer is measured using a dual-channel digital oscilloscope. The bandwidth, sampling rate, and vertical resolution of the oscilloscope (ISDS220B) are, respectively, 60 MHz, 200 MS/s and 8 bit. So, a high-precision voltage measurement could be guaranteed. The
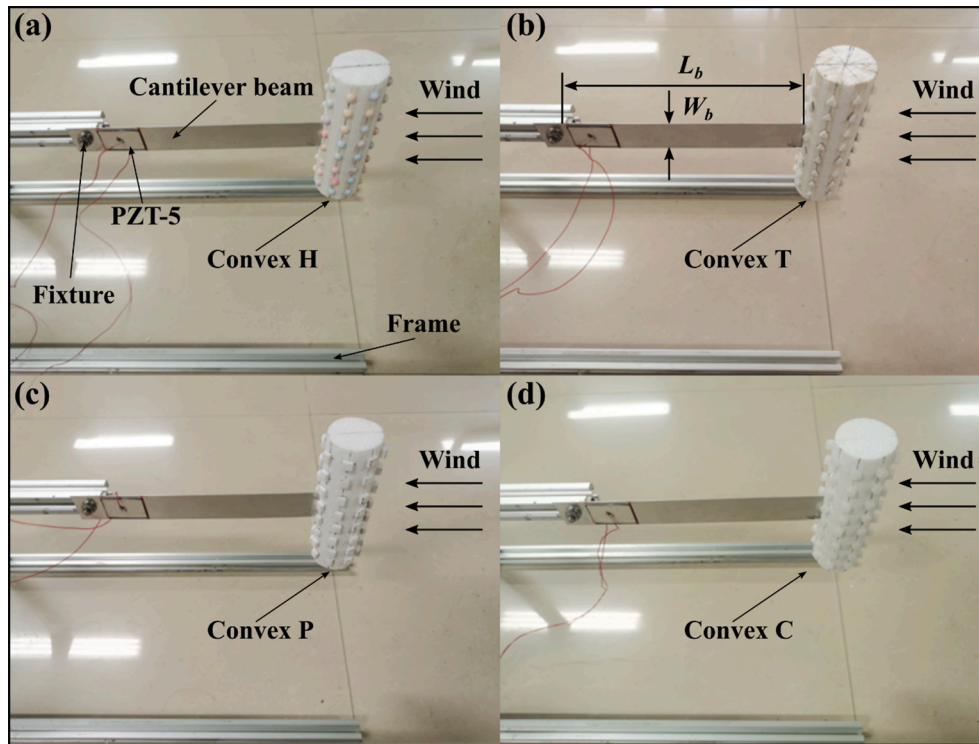
Fig. 10. Physical prototypes of VIVPEH with various metasurface bluff bodies.

Table 4
The system parameters of the VIVPEH prototype.

Properties	Value
M_{eff}	4.316 g
ω_n	47.87 rad/s
K_{eff}	9.894 N/m
C_{eff}	0.0096 N/(m/s)
θ	6.5×10^{-6} N/V
ξ	0.0233
C_p	12.2 (nF)

Table 5
The coefficients of different bluff body surfaces.

Bluff body surface	C_{L0}	C_D	S_t
Smooth surface	0.490	1.331	0.128
Convex prism	0.568	1.539	0.142
Convex cylinder	0.549	1.544	0.137
Convex tri-prism	0.544	1.546	0.121
Convex hemisphere	0.551	1.495	0.115

displacement of the bluff body is measured by a laser sensor (Panasonic: HG-C1400) with a repeatability resolution of 300 μm. In the experiment, the laser sensor measures the center of the bluff body. The wind speed is gauged by a hot wire anemometer (Testo Co., USA) which has a resolution of 0.001 m/s. The operational wind speed range of the wind tunnel is 0 m/s $\leq U \leq$ 7 m/s. A series of wind tunnel experiments under a flow with a turbulence intensity less than 1.0% are carried out. For each wind speed, the long-term steady-state time history responses of the voltage and displacement are recorded to evaluate the performance of the proposed VIVPEHs.

The VIVPEH with an ordinary cylinder bluff body is tested first as a baseline reference. Then, the experiments for the four VIVPEHs with different metasurface decorated bluff bodies, as shown in Fig. 10(a–d), are carried out. Since the mass of the bluff body is different when decorated by different metasurfaces, additional small masses with different weights are utilized to compensate the differences between different bluff bodies for a fair comparison. Note that, in the following experimental comparisons, only the bluff body is replaced, while other test conditions remain unchanged.

4. Experimental results and discussions

4.1. Comparison and validation

To validate the developed theoretical model (Eqs. (6)–(8)) in Section

2, the experimental results measured at different wind speeds are compared with the theoretical results under the same open-circuit condition. The system parameters of the VIVPEH prototype are listed in Table 4. The effective mass M_{eff} is the weighted sum of the masses of the bluff body and the cantilever beam. The damping ratio ξ and natural frequency ω_n can be determined through a free decay test. The effective stiffness can then be obtained by $K_{eff} = \omega_n^2 M_{eff}$ and the effective damping can be obtained by $C_{eff} = 2\xi\omega_n M_{eff}$. The coefficients of bluff bodies with different surfaces used in the theoretical simulation are listed in Table 5.

Figs. 11 and 12, respectively, demonstrate the root mean square (RMS) output voltage V_{rms} from the VIVPEHs and the non-dimensional displacement amplitude y_{max}/D of the bluff bodies. It can be seen that both theoretical and experimental results are, in general, consistent over the wind speed range of $U = 0.8 \sim 4.1$ m/s. In addition, compared with the ordinary cylinder bluff body with a smooth surface, it can be found that the bluff bodies with convex T and H patterns can enhance the VIV over a wider wind speed range. While, the bluff bodies with convex P and C patterns can, by contrast, suppress the VIV, i.e., the lock-in region is reduced. Besides, it is also seen that for the cases "Convex T" and "Convex H", the Strouhal number S_t is smaller than that of the case "ordinary cylinder". While, the cases "Convex P" and "Convex C", the Strouhal number S_t is larger than that of the case "ordinary cylinder". The result indicates that smaller S_t can enhance the VIV, but higher S_t can suppress the VIV.

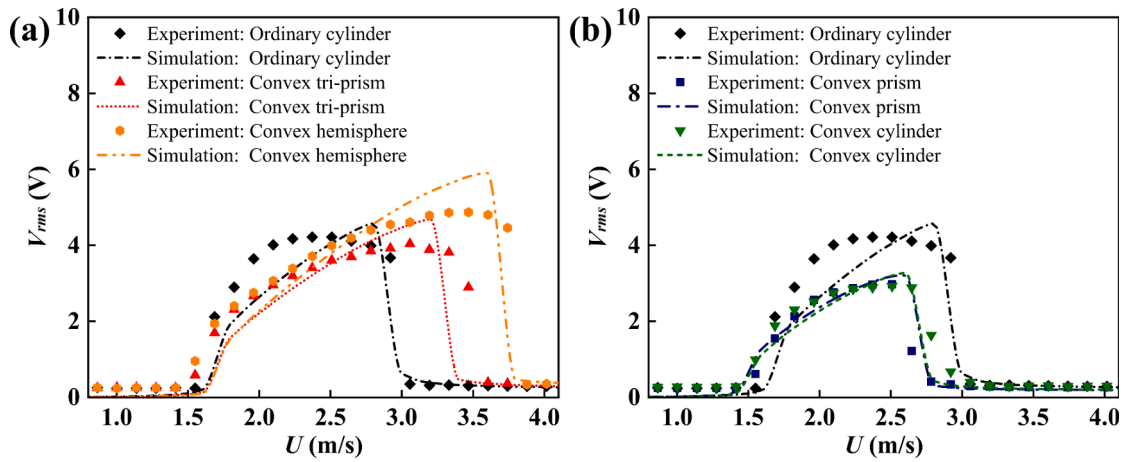The Strouhal number S_t is a dimensionless parameter defined as $S_t = $

Fig. 11. The theoretical and experimental results of the RMS voltage outputs of the VIVPEHs with different bluff bodies.
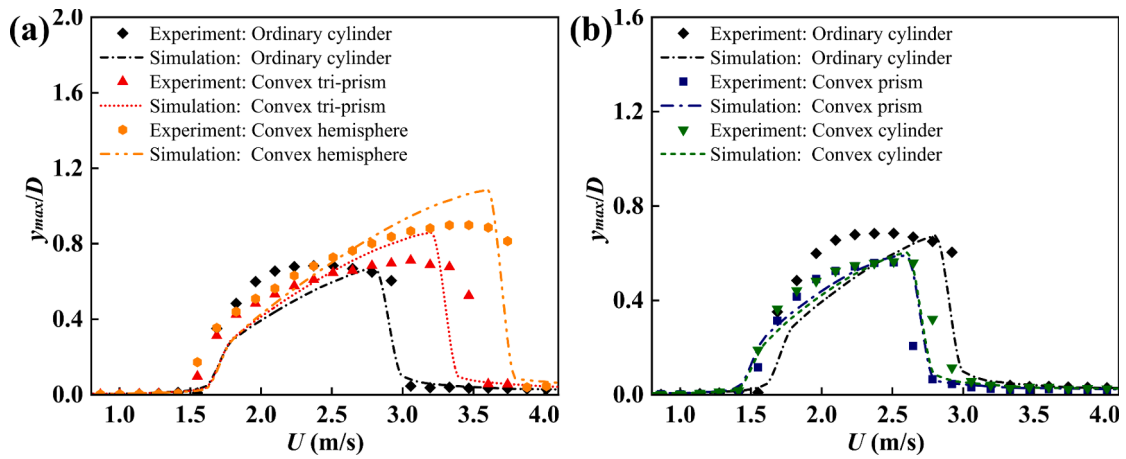

Fig. 12. The theoretical and experimental results of the non-dimensional displacement amplitudes of the VIVPEHs with different bluff bodies.

$f_s D/U$, where f_s is the vortex shedding frequency, D and U are the diameter of the bluff body and the incoming flow velocity, respectively. It describes the relationship between the vortex shedding frequency and the flow velocity. According to the mechanism of VIV, the system starts to lose the stability and oscillate mainly due to the aerodynamic force induced negative damping phenomenon. The vortex shedding frequency is first smaller than that of the resonant frequency of the system. With the increase of the wind speed, the vortex shedding frequency correspondingly increases. As the vortex shedding frequency approaches the resonant frequency of the system, the dynamic response amplitudes (i.e., the displacement and the voltage) increase. After the vortex shedding frequency exceed the resonant frequency of the system, the dynamic response amplitudes of the system decrease. When the vortex shedding frequency further increases to an extent, deviating far away from the resonant frequency of the system, the system stops oscillating, and returns to the static equilibrium state. Obviously, a smaller Strouhal number S_t could postpone the vortex shedding frequency exceeding the resonant frequency of the system. In other words, for a smaller Strouhal number S_t, the vortex shedding frequency approaches the resonant frequency of the system at a slower rate. Therefore, the above phenomenon that a smaller S_t could enhance VIV by widening the lock-in region, but a higher S_t leads to the reduction of the lock-in region for suppressing VIV, becomes physically interpretable. The following two subsections will present more details and discussions to give further insights into the two different situations.

4.2. Configurations towards vibration suppression

Under the same working condition, Fig. 13 presents the experimental results of the VIVPEHs with bluff bodies decorated by various metasurface patterns towards vibration suppression. As shown in Fig. 13(a, b), it is noted that both the convex P and C patterns could lead to the shrink of the lock-in region in terms of both the amplitude and the bandwidth, indicating the suppression of the vortex-induced vibration. Since the vibration is suppressed, according to Fig. 13(a), the non-dimensional displacement amplitudes of the bluff bodies with convex P and C patterns are 0.561 and 0.564, respectively. While the value of the case using an ordinary bluff body is 0.684. Besides, the maximum output voltages (as shown Fig. 13(b)) of the energy harvesters using bluff bodies decorated by convex P and C patterns are reduced to 2.975 V and 2.925 V, respectively. The maximum voltage output from that with the ordinary cylinder bluff body having a smooth surface is 4.215 V. Due to the use of the two metasurface decorated bluff bodies, the voltage outputs decrease by 29.42% and 30.61%, respectively. In addition to the vibration amplitudes, the wind speed range within which the VIV phenomenon can occur, i.e., the lock-in region, is also reduced. In fact, the decrease of the maximum displacement/voltage amplitude and the reduction of the effective wind speed range of VIV are closely correlated, both resulting from the higher Strouhal number S_t. As aforementioned in Section 4.1 that the Strouhal number S_t of the bluff bodies with convex P and C patterns are larger than that of the conventional one with a smooth surface. The vortex shedding frequency thus increases at a faster rate in pace with the increase of the wind speed.
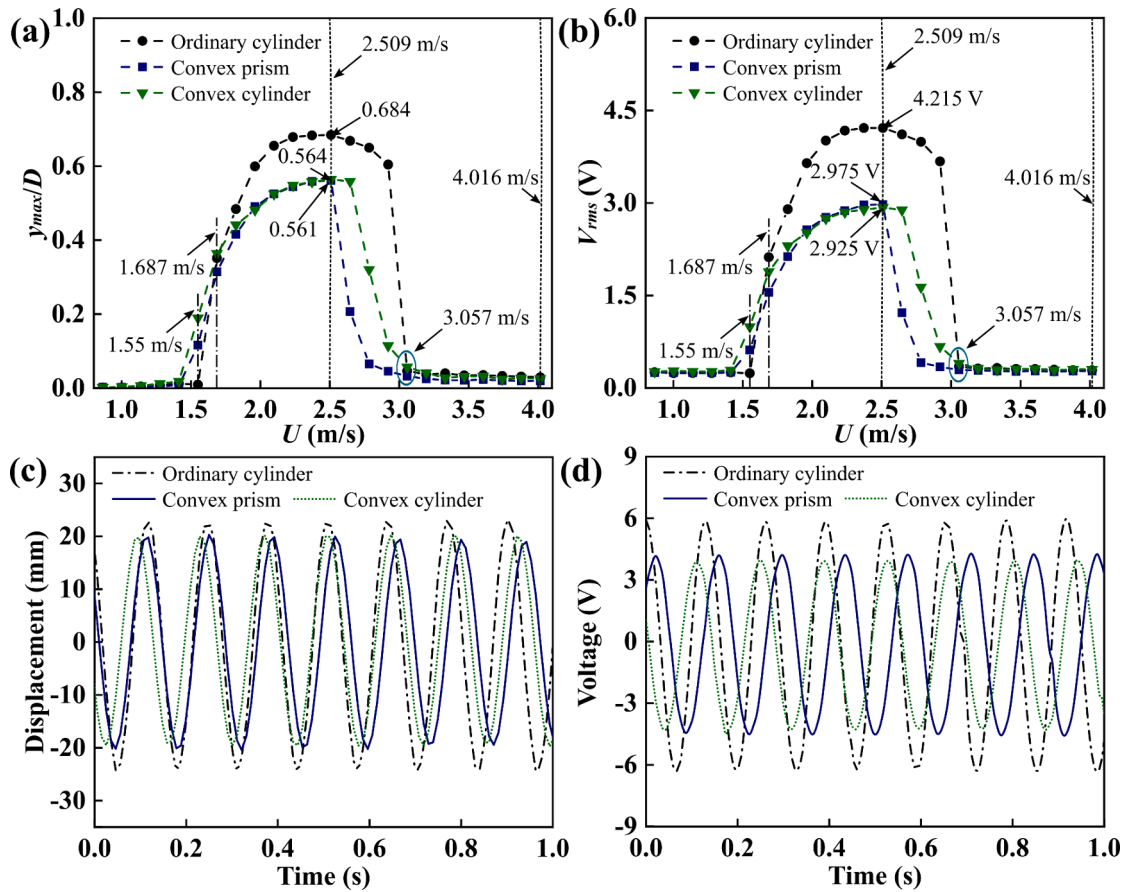
Fig. 13. The experimental results of the VIVPEHs with the bluff bodies decorated by convex P and C patterns: (a) non-dimensional displacement amplitude versus wind speed; (b) RMS voltage output versus wind speed; time history responses of (c) displacement and (d) voltage at $U = 2.509$ m/s.

Consequently, the matching between the vortex shedding frequency and the system resonant frequency happens at a lower wind speed. From Eq. (6), it is known that the aerodynamic force is proportional to the wind speed. Therefore, when the vortex shedding frequency and the system resonant frequency are exactly aligned, i.e., the resonance takes place, at a lower wind speed, the corresponding aerodynamic force is smaller. As a result, the voltage output from the piezoelectric transducer is smaller.

The time history responses of the three kinds of bluff bodies at the specific wind speed of $U = 2.509$ m/s are presented in Fig. 13(c) and (d). It is worth mentioning that $U = 2.509$ m/s corresponds to the optimal wind speed, under which both the vibration amplitude and the output voltage reach their maximums. The results show that the oscillations of all the three energy harvesters with different bluff bodies are mono-periodic. Moreover, it is clearly observed that the displacement/voltage amplitudes of the two energy harvesters with metasurface decorated bluff bodies are smaller.

4.3. Configurations towards energy harvesting

From the perspective of energy harvesting, it is preliminary learned that the bluff bodies decorated by convex T and H patterns can enhance the lock-in phenomenon by increasing both the response amplitude and the operation bandwidth. Under the same working condition, the corresponding results of the energy harvesters with these two bluff bodies are presented in Fig. 14. The results of the conventional energy harvester using an ordinary bluff body are also provided for ease of comparison. As revealed in Fig. 14(a), from the point of view of the non-dimensional displacement amplitude, the maximum amplitude of the energy harvester with the bluff body decorated by the convex H pattern (0.899) is greater than that of the conventional energy harvester (0.684) for

about 31.43%. According to Fig. 14(b), the maximum voltage amplitude of the conventional energy harvester is about 4.215 V. The maximum voltage amplitude of the energy harvester with the bluff body decorated by the convex H pattern is about 4.871 V, indicating an increase of 15.56% as compared to that of the conventional energy harvester.

In addition, from the perspective of the operation bandwidth, i.e., the width of the lock-in region, the effective bandwidths of the two energy harvesters with bluff bodies decorated by convex T and H patterns are $1.413 \sim 3.605$ m/s and $1.413 \sim 3.879$ m/s, respectively. In comparison, the effective bandwidth of the conventional energy harvester is only about $1.55 \sim 3.057$ m/s. Therefore, the energy harvesting performance is considerably enhanced due to the decoration of the bluff body by the two kinds of metasurface patterns. Similarly, the increase of the maximum displacement/voltage amplitude and the enlargement of the effective wind speed range of VIV for energy harvesting is not just a coincidence. The decrease of the Strouhal number S_t of the bluff bodies with convex T and H patterns is the underlying reason for the above two phenomena. As listed in Table 5, the Strouhal number S_t of the bluff bodies with convex T and H patterns are smaller than the conventional one with a smooth surface, indicating that the vortex shedding frequency increases at a slower rate in pace with the increase of the wind speed. One can easily deduce that the exact resonance takes place at a higher wind speed under the excitation of a larger aerodynamic force. Therefore, the maximum voltage output obtained at this condition is larger.

Fig. 14(c) and (d) further present the time history responses of the energy harvesters using the three kinds of bluff bodies. One can note that compared with the conventional energy harvester, the voltage amplitude of the energy harvester with the bluff body decorated by the convex H pattern is evidently larger, while that of the energy harvester with the
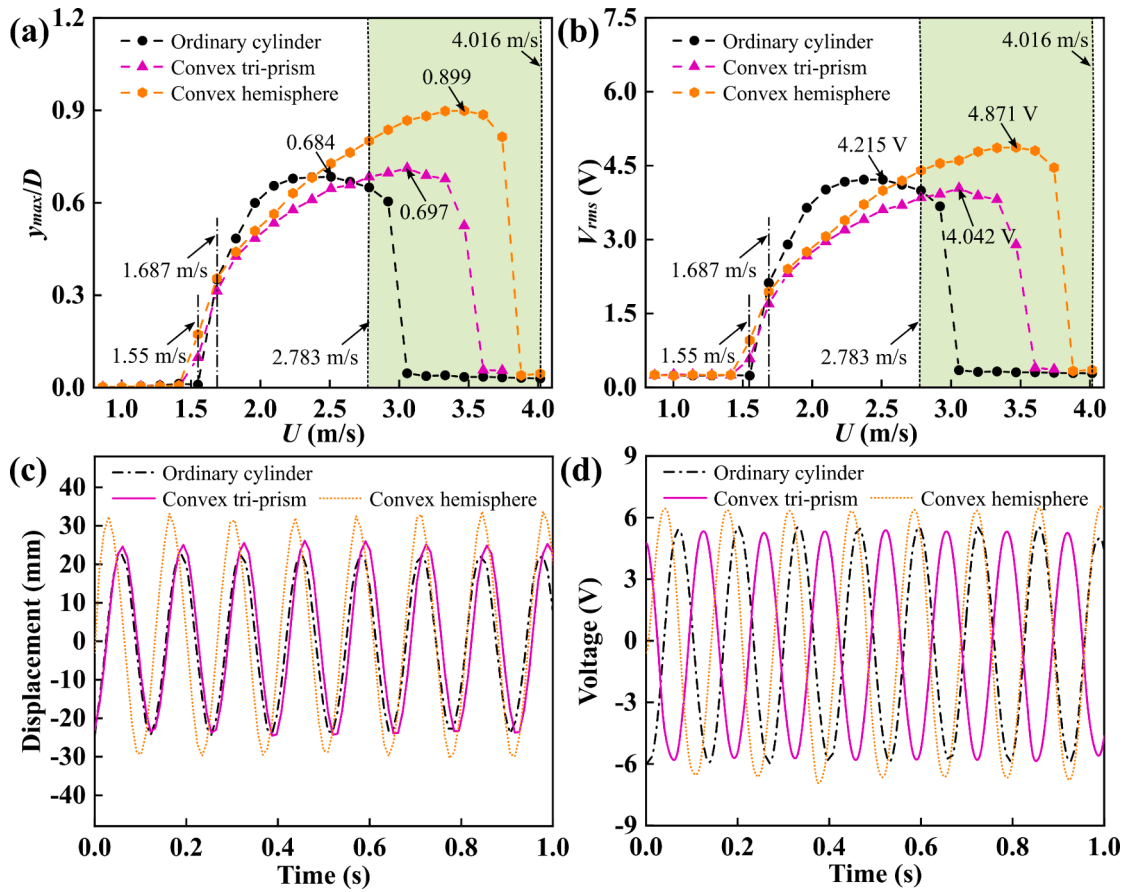
Fig. 14. The experimental results of the VIVPEHs with the bluff bodies decorated by convex T and H patterns: (a) non-dimensional displacement amplitude versus wind speed; (b) RMS voltage output versus wind speed; time history responses of (c) displacement and (d) voltage at $U = 2.783$ m/s.
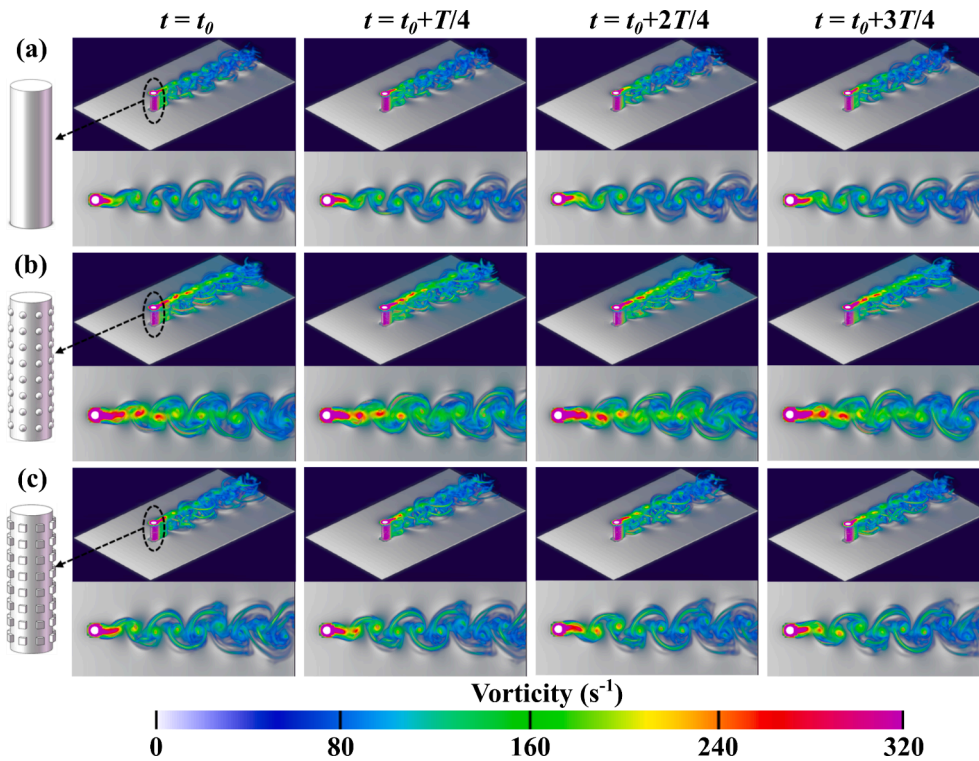

Fig. 15. Vorticity contours obtained from CFD simulation to illustrate the vortex shedding processes around: (a) the ordinary cylinder bluff body; (b) the bluff body decorated by convex H pattern; (c) the bluff body decorated by convex P pattern.
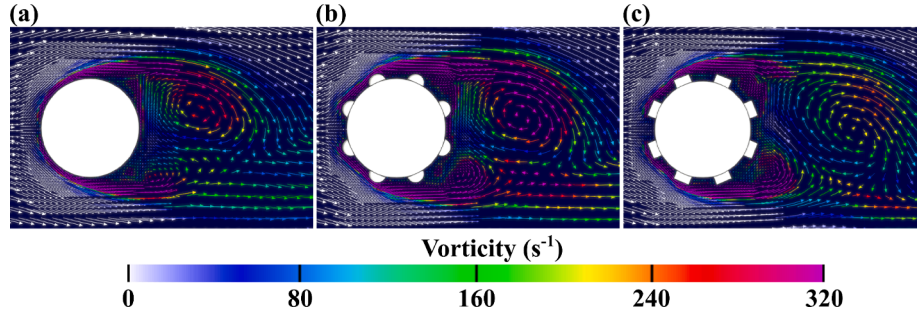
Fig. 16. Vorticity vectors obtained from CFD simulation to illustrate the near-filed flow around: (a) the ordinary cylinder bluff body; (b) the bluff body decorated by convex H pattern; and (c) the bluff body decorated by convex P pattern.

bluff body decorated by the convex T pattern is slightly smaller.

5. Further simulation and theoretical analysis

5.1. Analysis of the flow field

To help better understand the influences of various metasurfaces on the aerodynamics of the system, Fig. 15 shows the vorticity contours obtained from the CFD simulation around the bluff bodies with different characteristics to illustrate the vortex shedding processes. In the figure, T represents a certain time length that equals the period of the vortex shedding cycle. As shown in Fig. 15, compared with the ordinary cylinder bluff body, more fierce vortices behind the bluff body decorated by the convex H pattern are observed. The vortex strength maintains at a larger level than that of the ordinary cylinder bluff body at different vortex shedding locations. The mechanism behind this phenomenon can be potentially explained by that the existence of the periodic convex H pattern forces the flow field to vary more violently, resulting in a dramatic pressure variation in the wake flow. The vortex-induced vibration and, consequently, the energy harvesting performance is enhanced. However, the vortex behind the bluff body decorated by the convex P pattern is smaller, and the vortices become weaker at an earlier position, which is manifested in the dissipation of vortex in advance and the slower vortex shedding, implying that this metasurface is beneficial for suppressing the vortex-induced vibration. Fig. 16 demonstrates the vorticity vectors obtained from CFD simulation to illustrate the near-field flows around various bluff bodies with different surface features. As can be seen in Fig. 16, the existence of metasurfaces could alter the flow field around the bluff bodies. Compared with the ordinary cylinder bluff body, the boundary layer separation of the flow takes place at a faster rate near the bluff body decorated by the convex H pattern, and the vortices are stronger. That is why the convex H pattern metasurface could promote the VIV phenomenon for benefiting energy harvesting. By contrast, the near-wall fluid attachment of the bluff body decorated by the convex P pattern is stronger. Hence, the boundary layer separation takes place at a slower rate, and the generated vortices are weaker.
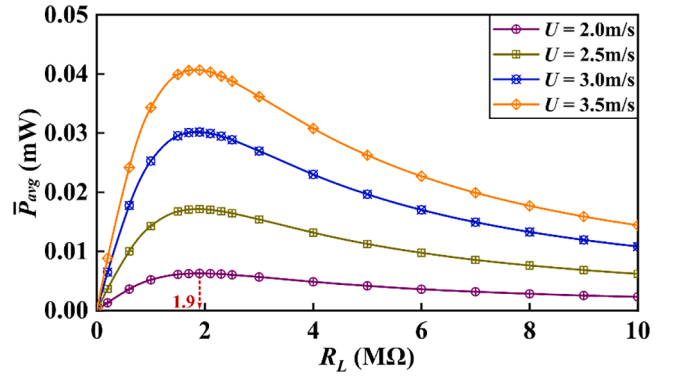

Fig. 18. The averaged power versus the resistive load under different wind speeds.

This explains why the convex P pattern metasurface could suppress VIV and deteriorate the energy harvesting performance.

5.2. Parametric study

To investigate the effects of the resistive load R_L and the electromechanical coupling strength on the performance of the energy harvester, the validated theoretical model presented in Section 2 is employed to perform a parametric study. In the following study, the averaged power and the electromechanical coupling strength are, respectively, defined by the below formula:

$$\overline{P}_{avg} = \frac{V_{rms}^2}{R_L} \tag{16}$$

$$k_e^2 = \frac{\theta^2}{C_p K_{eff}} \tag{17}$$

Without loss of generality but to avoid redundancy, only the energy
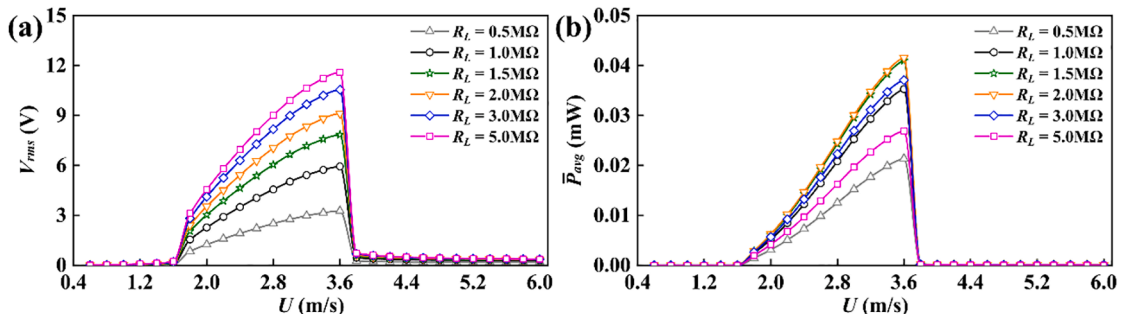

Fig. 17. (a) The RMS output voltage and (b) the averaged power versus wind speed under different resistive loads.
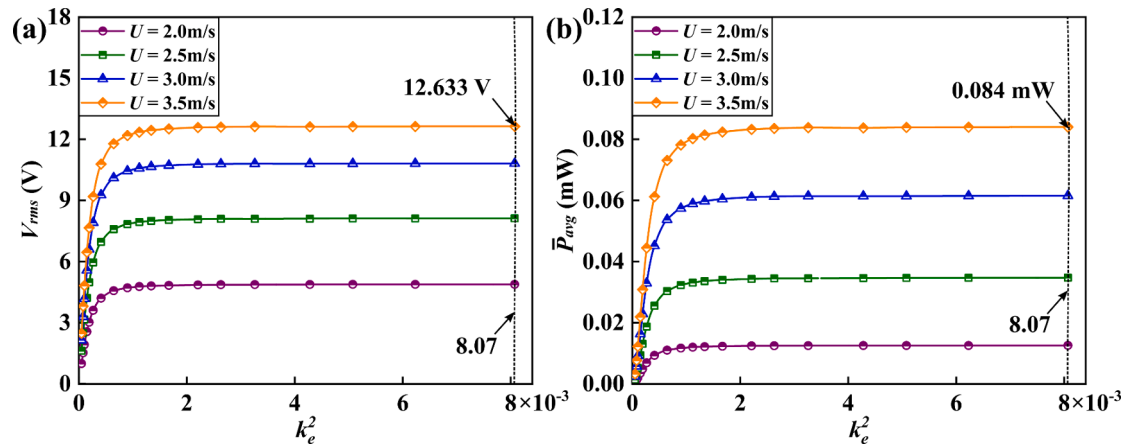
Fig. 19. (a) The RMS output voltage and (b) the averaged power versus the electromechanical coupling strength k_e^2 under different wind speeds.

harvester with the bluff body decorated by the convex H pattern is analyzed. The investigation of other energy harvesters can follow the same analysis procedures and criteria. By varying the wind speed, Fig. 17 demonstrates the variations of the RMS output voltage and the averaged power on different R_L. From Fig. 17(a), it is noted that the RMS output voltage increases monotonically with the increase of the R_L. However, Fig. 17(b) shows that under the same wind speed, the averaged power first increases and then decreases with the increase of R_L. It can be deduced that the optimal R_L is in the range of $1.5 \sim 2.0$ MΩ. To further seek the optimal R_L, Fig. 18 shows the averaged power versus R_L under different wind speeds. It is clearly revealed that under a specific wind speed there appears a peak. For instance, under the wind speed of $U = 3.5$ m/s, the maximum averaged power that can be achieved is 0.041 mW by shunting to the optimal resistive load of $R_{L0} = 1.9$ MΩ.

Once the mechanical structure of an energy harvester is manufactured, the electromechanical coupling strength is another one of the few factors that can influence the energy harvesting performance. Under different wind speeds, Fig. 19 presents the variations of the RMS output voltage and averaged power with the change of the electromechanical coupling strength. It is worth mentioning that the change of electromechanical coupling strength is realized by varying the capacitance, while keeping the electromechanical coupling coefficient θ as constant.

The results show that the RMS output voltage and averaged power both increase with the increase of k_e^2 and approach to constant values when k_e^2 becomes sufficiently large. To give a quantitative example, when k_e^2 is 8.07×10^{-3} and the wind speed is 3.5 m/s, the maximum RMS output voltage is 12.633 V and the maximum averaged power is about 0.084 mW. An appropriate increase of the electromechanical coupling strength can improve the energy harvesting performance. However, arbitrarily increasing the electromechanical coupling strength is unnecessary and would not bring any further benefits for energy harvesting, but poses difficulties in manufacturing the piezoelectric transducer.

6. Conclusions

This paper has proposed and investigated four kinds of bluff bodies decorated by various metasurface patterns towards either vortex-induced vibration suppression or energy harvesting. A theoretical model has been developed for predicting the dynamic behaviors of the proposed VIV systems. The lift and drag coefficients used in the theoretical model are determined from the CFD simulation using the Lattice-Boltzmann method. The vorticity contours have been obtained from the CFD simulation to illustrate the vortex shedding processes affected by various metasurface patterns. A wind tunnel experimental study has been conducted to examine the dynamic behaviors and the energy harvesting performance of the energy harvesters using various

metasurface decorated bluff bodies. It has revealed that by only slightly modifying the surface of the bluff body without the need to transform its cross-section profile, the aerodynamic characteristics could be significantly changed and customized for different application purposes.

According to the experimental results, the bluff bodies with convex tri-prism and convex hemisphere patterns can enhance vortex-induced vibration by enlarging the lock-in region. Thus, they are beneficial for energy harvesting. The maximum voltage and displacement amplitudes of the energy harvester using the bluff body decorated by the convex hemisphere pattern are increased by 15.56% and 31.34%, respectively. Moreover, the lock-in region is increased by 63.64% compared with that using a bluff body with a smooth surface. By contrast, the bluff bodies with convex prism and convex cylinder patterns can suppress the vortex-induced vibration. In a given instance, using the two bluff bodies lead to the reduction of the non-dimensional displacement amplitude by 17.98% and 17.54%, respectively. The lock-in region is slightly decreased.

Based on the developed theoretical model that has been validated by the experiment, a parametric study has been performed to investigate the effects of the load resistance, and the electromechanical coupling strength on the energy harvesting performance. The energy harvesting performance can be improved by increasing the electromechanical coupling strength to a reasonable level, but the power output saturates with extremely large coupling strength. Since the price of a piezoelectric element with a large coupling coefficient is often high, it is recommended to choose a piezoelectric element with a moderate coupling coefficient from the cost-effective perspective.

CRediT authorship contribution statement

Junlei Wang: Conceptualization, Investigation, Formal analysis, Writing - original draft, Funding acquisition. **Shaokang Sun:** Writing - original draft. **Lihua Tang:** Conceptualization, Supervision, Writing - review & editing. **Guobiao Hu:** Investigation, Formal analysis, Writing - review & editing. **Junrui Liang:** Writing - review & editing.

Declaration of Competing Interest

The authors declare that they have no known competing financial interests or personal relationships that could have appeared to influence the work reported in this paper.

Acknowledgments

and Soyotec Technologies Co., Ltd. (Beijing) on XFlow Software.

References

[1] Priya S, Inman DJ. Energy Harvesting Technologies. New York: Springer; 2009.

[2] Zhao L-C, Zou H-X, Yan G, Liu F-R, Tan T, Wei K-X, et al. Magnetic coupling and flextensional amplification mechanisms for high-robustness ambient wind energy harvesting. Energy Convers Manage 2019;201:112166.

[3] Rantz R, Halim M, Xue T, Zhang Q, Gu L, Yang K, et al. Architectures for wrist-worn energy harvesting. Smart Mater Struct 2018;27(4):044001.

[4] Zou H-X, Zhao L-C, Gao Q-H, Zuo L, Liu F-R, Tan T, et al. Mechanical modulations for enhancing energy harvesting: Principles, methods and applications. Appl Energy 2019;255:113871.

[5] Zhang Z, Wang S, Kan J, Hu W, Chen Z, Xu H. A pneumatic piezoelectric vibration energy harvester based on the compressed air-transducer-structure interaction. Energy Convers Manage 2020;213:112861.

[6] Guo X, Zhang Y, Fan K, Lee C, Wang F. A comprehensive study of non-linear air damping and "pull-in" effects on the electrostatic energy harvesters. Energy Convers Manage 2020;203:112264.

[7] Zhao D, Hu X, Tan T, Yan Z, Zhang W. Piezoelectric galloping energy harvesting enhanced by topological equivalent aerodynamic design. Energy Convers Manage 2020;222:113260.

[8] Sun W, Seok J. A novel self-tuning wind energy harvester with a slidable bluff body using vortex-induced vibration. Energy Convers Manage 2020;205:112472.

[9] Song D, Zheng S, Yang S, Yang J, Dong M, Su M, et al. Annual Energy Production Estimation for Variable-Speed Wind Turbine at High-Altitude Site. J Modern Power Syst Clean Energy 2020.

[10] Abdelkefi A. Aeroelastic energy harvesting: A review. Int J Eng Sci 2016;100: 112–35.

[11] Wang J, Geng L, Ding L, Zhu H, Yurchenko D. The state-of-the-art review on energy harvesting from flow-induced vibrations. Appl Energy 2020;267:114902.

[12] BlevinS RD. Flow induced vibration, 1990. Naudascher: E., Rockwell, D., Flow Induced Vibrations; 1994.

[13] Bernitsas MM, Raghavan K, Ben-Simon Y, Garcia E. VIVACE (Vortex Induced Vibration Aquatic Clean Energy): A new concept in generation of clean and renewable energy from fluid flow. J Offshore Mech Arct Eng 2008;130(4).

[14] Williamson CH, Roshko A. Vortex formation in the wake of an oscillating cylinder. J Fluids Struct 1988;2(4):355–81.

[15] Barrero-Gil A, Alonso G, Sanz-Andres A. Energy harvesting from transverse galloping. J Sound Vib 2010;329(14):2873–83.

[16] Sirohi J, Mahadik R. Harvesting wind energy using a galloping piezoelectric beam. J Vib Acoust 2012;134(1).

[17] Hémon P, Amandolese X, Andrianne T. Energy harvesting from galloping of prisms: A wind tunnel experiment. J Fluids Struct 2017;70:390–402.

[18] Eugeni M, Elahi H, Fune F, Lampani L, Mastroddi F, Romano GP, et al. Numerical and experimental investigation of piezoelectric energy harvester based on flag-flutter. Aerosp Sci Technol 2019:105634.

[19] Elahi H, Eugeni M, Fune F, Lampani L, Mastroddi F, Paolo Romano G, et al. Performance evaluation of a piezoelectric energy harvester based on flag-flutter. Micromachines 2020;11(10):933.

[20] Alhadidi A, Daqaq M. A broadband bi-stable flow energy harvester based on the wake-galloping phenomenon. Appl Phys Lett 2016;109(3):033904.

[21] Rezaei M, Talebitooti R. Wideband PZT energy harvesting from the wake of a bluff body in varying flow speeds. Int J Mech Sci 2019;163:105135.

[22] Torres EO, Rincón-Mora GA. Electrostatic energy-harvesting and battery-charging CMOS system prototype. IEEE Trans Circuits Syst I Regul Pap 2008;56(9):1938–48.

[23] Khan FU, Qadir MU. State-of-the-art in vibration-based electrostatic energy harvesting. J Micromech Microeng 2016;26(10):103001.

[24] Fan K, Cai M, Liu H, Zhang Y. Capturing energy from ultra-low frequency vibrations and human motion through a monostable electromagnetic energy harvester. Energy 2019;169:356–68.

[25] Dal Bo L, Gardonio P, Turco E. Analysis and scaling study of vibration energy harvesting with reactive electromagnetic and piezoelectric transducers. J Sound Vib 2020;484.

[26] Erturk A, Inman DJ. On mechanical modeling of cantilevered piezoelectric vibration energy harvesters. J Intell Mater Syst Struct 2008;19(11):1311–25.

[27] Khazaee M, Rosendahl L, Rezania A. A comprehensive electromechanically coupled model for nonuniform piezoelectric energy harvesting composite laminates. Mech Syst Sig Process 2020;145:26.

[28] Hu G, Wang J, Tang L. A comb-like beam based piezoelectric system for galloping energy harvesting. Mech Syst Sig Process 2021;150:107301.

[29] Toprak A, Tigli O. Piezoelectric energy harvesting: State-of-the-art and challenges. Appl Phys Rev 2014;1(3):031104.

[30] Lai Z, Wang S, Zhu L, Zhang G, Wang J, Yang K, et al. A hybrid piezo-dielectric wind energy harvester for high-performance vortex-induced vibration energy harvesting. Mech Syst Sig Process 2021;150:107212.

[31] Jo S-H, Yoon H, Shin YC, Youn BD. An analytical model of a phononic crystal with a piezoelectric defect for energy harvesting using an electroelastically coupled transfer matrix. Int J Mech Sci 2021;193:106160.

[32] Zhang L, Meng B, Xia Y, Deng Z, Dai H, Hagedorn P, et al. Galloping Triboelectric Nanogenerator for Energy Harvesting under Low Wind Speed. Nano Energy 2020; 70:104477.

[33] Khan U, Kim S-W. Triboelectric nanogenerators for blue energy harvesting. ACS Nano 2016;10(7):6429–32.

[34] Hinchet R, Yoon H-J, Ryu H, Kim M-K, Choi E-K, Kim D-S, et al. Transcutaneous ultrasound energy harvesting using capacitive triboelectric technology. Science 2019;365(6452):491–4.

[35] Zhu H, Li G, Wang J. Flow-induced vibration of a circular cylinder with splitter plates placed upstream and downstream individually and simultaneously. Appl Ocean Res 2020;97:102084.

[36] Xu W, Ji C, Sun H, Ding W, Bernitsas MM. Flow-induced vibration of two elastically mounted tandem cylinders in cross-flow at subcritical Reynolds numbers. Ocean Eng 2019;173:375–87.

[37] Williamson C, Govardhan R. A brief review of recent results in vortex-induced vibrations. J Wind Eng Ind Aerodyn 2008;96(6–7):713–35.

[38] Dai HL, Abdelkefi A, Wang L. Theoretical modeling and nonlinear analysis of piezoelectric energy harvesting from vortex-induced vibrations. J Intell Mater Syst Struct 2014;25(14):1861–74.

[39] Azadeh-Ranjbar V, Elvin N, Andreopoulos Y. Vortex-induced vibration of finite-length circular cylinders with spanwise free-ends: Broadening the lock-in envelope. Phys Fluids 2018;30(10).

[40] M.M. Bernitsas and K. Raghavan, Enhancement of vortex induced forces and motion through surface roughness control. 2011, Vortex Hydro Energy LLC.

[41] Wang J, Zhao G, Zhang M, Zhang Z. Efficient study of a coarse structure number on the bluff body during the harvesting of wind energy. Energy Sources Part A 2018; 40(15):1788–97.

[42] Wang J, Zhou S, Zhang Z, Yurchenko D. High-performance piezoelectric wind energy harvester with Y-shaped attachments. Energy Convers Manage 2019;181: 645–52.

[43] Hu G, Tse KT, Kwok KCS, Song J, Lyu Y. Aerodynamic modification to a circular cylinder to enhance the piezoelectric wind energy harvesting. Appl Phys Lett 2016; 109(19):193902.

[44] He X, Yang X, Jiang S. Enhancement of wind energy harvesting by interaction between vortex-induced vibration and galloping. Appl Phys Lett 2018;112(3): 033901.

[45] Sun W, Jo S, Seok J. Development of the optimal bluff body for wind energy harvesting using the synergetic effect of coupled vortex induced vibration and galloping phenomena. Int J Mech Sci 2019;156:435–45.

[46] Wang J, Gu S, Zhang C, Hu G, Chen G, Yang K, et al. Hybrid wind energy scavenging by coupling vortex-induced vibrations and galloping. Energy Convers Manage 2020;213:112835.

[47] Ji-ning S, Lin LV, Jian-qiao Z, Hao WU, Guo-qiang T, Guang-wei LI, et al. Experimental investigation of suppression of vortex-induced vibration of marine risers by three control rods. Ocean Eng 2009;27(3):23–9.

[48] Zhu H, Gao Y. Vortex-induced vibration suppression of a main circular cylinder with two rotating control rods in its near wake: Effect of the rotation direction. J Fluids Struct 2017;74:469–91.

[49] Shalaginov MY, Campbell SD, An SS, Zhang YF, Rios C, Whiting EB, et al. Design for quality: reconfigurable flat optics based on active metasurfaces. Nanophotonics 2020;9(11):3505–34.

[50] Kildishev AV, Boltasseva A, Shalaev VM. Planar photonics with metasurfaces. Science 2013;339:6125.

[51] Esfahlani H, Lissek H, Mosig JR. Generation of acoustic helical wavefronts using metasurfaces. Phys Rev B 2017;95(2):024312.

[52] Miyata K, Noguchi Y, Yamada T, Izui K, Nishiwaki S. Optimum design of a multi-functional acoustic metasurface using topology optimization based on Zwicker's loudness model. Comput Methods Appl Mech Eng 2018;331:116–37.

[53] Zaccherini R, Colombi A, Palermo A, Dertimanis VK, Marzani A, Thomsen HR, et al. Locally resonant metasurfaces for shear waves in granular media. Phys Rev Appl 2020;13(3).

[54] Liu W, Yoon GH, Yi B, Yang Y, Chen Y. Ultra-wide band gap metasurfaces for controlling seismic surface waves. Extreme Mech Lett 2020;41:101018.

[55] Mou Z, Lu XQ, Lv HR, Han YS, Yue QY, Wang SY, et al. Metasurface array illuminator based on fresnel holography. Opt Lasers Eng 2020;131:4.

[56] Long H, Liu C, Shao C, Cheng Y, Chen K, Qiu X, et al. Subwavelength broadband sound absorber based on a composite metasurface. Sci Rep 2020;10(1):1–10.

[57] He Y, Chen T, Song X. Manipulation of seismic Rayleigh waves using a phase-gradient rubber metasurface. Int J Mod Phys B 2020;34(13):2050142.

[58] Erturk A, Inman DJ. Issues in mathematical modeling of piezoelectric energy harvesters. Smart Mater Struct 2008;17(6):065016.

[59] Facchinetti ML, De Langre E, Biolley F. Coupling of structure and wake oscillators in vortex-induced vibrations. J Fluids Struct 2004;19(2):123–40.

[60] Wang J, Tang L, Zhao L, Zhang Z. Efficiency investigation on energy harvesting from airflows in HVAC system based on galloping of isosceles triangle sectioned bluff bodies. Energy 2019;172:1066–78.

[61] Bhatnagar PL, Gross EP, Krook M. A model for collision processes in gases. I. Small amplitude processes in charged and neutral one-component systems. Phys Rev 1954;94(3):511.

[62] S.L. Han, R.X. Yu, Z.Y. Li, and Y.Y. Wang. Effect of Turbulence Model on Simulation of Vehicle Aerodynamic Characteristics Based on XFlow. Applied Mechanics and Materials. 2014. Trans Tech Publ.